

A Novel Series of Single-Cluster Catalysts: Transition Metal Trimer Clusters Supported on Graphdiyne

Jin-Cheng Liu[†], Hai Xiao[†], Xiao-Kun Zhao[†], Nan-Nan Zhang[†], Yuan Liu^{†,§}, Deng-Hui Xing[†],
Xiaohu Yu[‡], Han-Shi Hu[†], Jun Li^{*,†,§}

[†] Department of Chemistry and Key Laboratory of Organic Optoelectronics & Molecular Engineering of Ministry of Education, Tsinghua University, Beijing 100084, China

[‡] Shaanxi Key Laboratory of Catalysis and School of Chemical & Environment Sciences, Shaanxi University of Technology, Hanzhong 723000, China

[§] Department of Chemistry, Southern University of Science and Technology, Shenzhen 518055, China

E-mail: junli@tsinghua.edu.cn

Abstract: While single-atom catalysts (SACs) have achieved great success in the past decade, their application is potentially limited by the simplistic single-atom active centers, which makes single-cluster catalysts (SCCs) a natural extension. SCCs with precise numbers of atoms and structural configurations possess SAC's merits, yet have greater potentials for catalyzing complex reactions and/or bulky reactants. Through systematic quantum-chemical studies and computational screening, we report here the rational design of transition metal trimer clusters anchored on graphdiyne as a novel kind of stable SCCs with great potentials for efficient and precise heterogeneous catalysis. By investigating their structures and catalytic performance for oxygen reduction reaction, hydrogen evolution reaction, and CO₂ reduction reactions, we provide theoretical guidelines for their potential applications as heterogeneous catalysts. These graphdiyne supported SCCs provide an ideal benchmark scaffold for rational design of precise catalysts for industrially important chemical reactions.

INTRODUCTION

In the past decade, single-atom catalysts (SACs) have emerged as the new frontier of heterogeneous catalysis, owing to their high performance with regards to atomic efficiency, selectivity, stability and activity, as well as precisely tunable quantum states through support manipulation.¹⁻⁵ However, SACs are not always an optimal design for complex reactions, such as those that require multi-step redox reactions (e.g. in photosynthesis and nitrogenase), interaction among two or more adsorbed bulky reactant molecules, or multiple functional sites (e.g., in order to break the cumbersome scaling relations).⁶ Recently, single-cluster catalysts (SCCs) with atomically precise active centers composed of well-defined stable clusters are proposed as a natural extension of SACs toward optimal design of complicated heterogeneous catalysts.⁶⁻¹⁴ However, the stability and thus the synthesis of SCCs pose a grand challenge, because a delicate balance is required to

prevent both further aggregation of the clusters to form nanoparticles and their dispersion to form single-atoms.

To form robust SCCs, a prototype material with natural pores or defect anchoring sites would be necessary. The synthesis of graphdiyne (GDY) by Li *et al.*¹⁵⁻¹⁸ presents an ideal substrate for hosting both SACs and SCCs as GDY has natural 6-membered rings (6MRs) and 18-membered rings (18MRs). There have been reports of metal/GDY complexes with various applications,¹⁹⁻²⁰ and the 18MR-hole of GDY was shown to provide a suitable site for anchoring metal (M) single-atom (SA) or single-cluster (SC) as heterogeneous catalyst.²¹ However, most of previous work on M/GDY focused on SAs. For example, non-noble metal Fe and Ni SAs anchored on GDY (denoted as Fe₁/GDY and Ni₁/GDY) were shown to perform better for hydrogen evolution reaction (HER) than the commercial Pt/C.²¹ By first-principle calculations, Li *et al.* investigated the stability and electronic structures of M₁/GDY with M = from Sc to Zn.²² Additionally, Mo₁/GDY,²³ Ir₁/GDY,²⁴ W₁/N-doped GY,²⁵ Pt₁/GDY,²⁶ Fe₁/GDY,²⁷ AM₁/GDY²⁸, TM₁/GDY²⁹ (AM = alkali metal, TM = transition metal) were theoretically proposed as good catalysts for reactions including nitrogen fixation, CO oxidation, HER, oxygen reduction reaction (ORR), and water splitting reaction.

However, these studies on M₁/GDY did not explore the possibility that the SA form of metal on GDY might be less stable than its SC form, particularly when comparing with the highly stable triatomic cluster form.³⁰⁻³¹ Ma *et al.* reported diatomic cluster catalysts on GDY for nitrogen reduction reaction.³² Zhang *et al.* speculated that the triangular 18MR-hole of GDY can accommodate three Li atoms at the three symmetric corners with a unique triangular configuration, and the resulted Li₃/GDY can be used as anode material for lithium ion batteries.³³ Qi *et al.* investigated the performance of Pd clusters on GDY for catalytic reduction, but did not characterize the structures of Pd clusters.³⁴ Very recently, we showed that the Os₃/GDY is a potential catalyst for selective semi-hydrogenation of acetylene.³⁵ Moreover, we predicted that the M₃ form is indeed the most stable for Pt and Ni supported on GDY, and suggested an efficient strategy based on the electrochemical potential window (EcPW) to prepare them via an electrochemical route.³¹

The metal trimer SCCs have been reported to deliver excellent performance. For instance, the Ru₃ cluster supported on N-doped carbon material was shown to be an efficient catalyst for selective oxidation of alcohols.⁹ The Ag₃ cluster on alumina support was demonstrated with high activity and selectivity for direct propylene epoxidation.⁸ The [Cu₃(μ -O)₃]²⁺ cluster in mordenite was shown to exhibit a high reactivity towards activation of inert C–H bonds in methane.^{14, 36} By first-principles calculations, we predicted that the Fe₃ cluster supported on Al₂O₃ leads to an associative mechanism for low-temperature ammonia synthesis with a high turnover frequency.¹¹

However, besides the EcPW strategy suggested by us, there are no efficient and specific ways to prepare stable metal trimer SCCs, because of the delicate requirement on the interaction between

metal and support. If the metal-support bonding is much stronger than the metal-metal bonding, the metal trimer SC will dissociate to form SAs. If the metal-support interaction is much weaker than the metal-metal bonding, the metal trimer SCs will aggregate into bigger clusters or nanoparticles. Thus, it is a prerequisite for a support for hosting the metal trimer SCC to balance the metal-metal and metal-support bonding strengths.

In this work, we investigate the viability of GDY as a support for TM trimer SCCs from both thermodynamic and kinetic aspects by first-principles calculations. Totally 13 late TM elements are considered. We further analyze the geometries and electronic structures of M_3/GDY , by taking Cu_3/GDY and Pt_3/GDY as two typical examples. At last, we investigate the catalytic performance of these M_3/GDY SCCs for ORR, HER, and CO_2 reduction reaction (CO_2RR), the results of which thus provide guidelines for their practical applications as heterogeneous catalysts.

COMPUTATIONAL DETAILS

All density functional theory (DFT) calculations were performed using the projector-augmented wave (PAW) method,³⁷ as implemented in the Vienna Ab initio Simulation Package (VASP) code.³⁸⁻³⁹ The spin-polarized Kohn-Sham formalism with gradient-corrected exchange and correlation functional of Perdew-Burke-Ernzerhof (PBE) flavor was adopted.⁴⁰ The cutoff energy of plane-wave basis sets was set to 400 eV. The Γ -point-only sampling was used for the Brillouin zone integration for the $\text{GDY}(2\times 2)$ -based models, which were adopted for energy calculations. And a $3\times 3\times 1$ Brillouin zone grid sampling was used for the $\text{GDY}(1\times 1)$ -based models, which were adopted for electronic structure analysis. All atoms as well as the lattice parameters \mathbf{a} and \mathbf{b} were allowed to relax for geometry optimization. The optimized lattice constant for pristine GDY we got is $|\mathbf{a}| = |\mathbf{b}| = 9.46 \text{ \AA}$, in good agreement with the previously reported value of 9.48 \AA by Long *et al.*⁴¹ The convergence criteria were set to be 10^{-6} eV and 0.01 eV/\AA for wavefunction and geometry optimization, respectively.

Free energy correction for all species was performed for ORR, HER, and CO_2RR reactions by vaspkit.⁴² For free molecules, the ideal gas approximation was assumed. For adsorbates, the contributions from all degrees of freedom to the free energies were treated as vibrations under the harmonic approximation, with unphysically low frequencies reset to a threshold of 60 cm^{-1} , which corresponds to the acoustic translational mode of the six-membered rings in water bulk.⁴³⁻⁴⁴

Ab initial molecular dynamics (AIMD) simulations were carried out for all $M_3/\text{GDY}(2\times 2)$. The AIMD calculations were started with the optimized configurations with lattice parameters fixed,

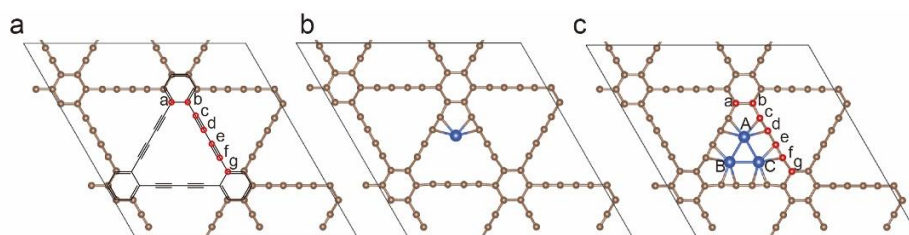
and were performed for more than 15 ps with a time step of 1 fs. The canonical (NVT) ensemble and Nosé-Hoover thermostats were employed with the temperature set to 300 K.⁴⁵⁻⁴⁶ Phonon dispersion was calculated using density-functional perturbation theory (DFPT),⁴⁷ as implemented in the VASP and analyzed by interfacing with the Phonopy code.⁴⁸

Band structures of GDY, Cu₃/GDY, and Pt₃/GDY were computed along the special line of Γ (0, 0, 0) \rightarrow M (0.5, 0.5, 0) \rightarrow X (0, 0.5, 0) \rightarrow Γ (0, 0, 0) at both PBE and Heyd-Scuseria-Ernzerhof (HSE06) levels.⁴⁹ Band decomposed charge densities were calculated at the Γ point for both the conduction band minimum (CBM) and valence band maximum (VBM) with degenerate bands summed up. Real space wavefunctions of CBM and VBM at the Γ point were extracted by vaspkit.⁴² The crystal orbital Hamilton population (COHP) analysis was performed with the LOBSTER 3.1.0 package, which reconstructs the orbital-resolved wavefunctions via projection of the delocalized plane waves to localized atomic-like basis sets.⁵⁰⁻⁵¹ The fragment molecular orbital (MO) analysis was performed using spin-restricted DFT with PBE and TZ2P Slater basis sets as implemented in the Amsterdam Density Functional (ADF) program.⁵² The frozen core approximation was applied to C[1s²] and Cu[1s²–2p⁶]. Relativistic effects were introduced by the zero-order regular approximation (ZORA) method. The optimized Cu₃/GDY molecular counterpart and its corresponding fragments (Cu₃ and GDY) were constrained to the D_{3h} symmetry.

RESULTS AND DISCUSSION

Stability of M₃/GDY.

Scheme 1a shows the structure of pristine GDY (the details are listed in **Table S1**), in which the length of C_c≡C_d bond (and its symmetric equivalents) is 1.227 Å, close to that in acetylene (1.20 Å), indicating a typical triple-bond character. There are six C≡C bonds bordering the 18MR-hole of GDY, but only two of them are involved in coordination with metal SA in reported M₁/GDY cases (**Scheme 1b**).²² While the remaining space of 18MR-hole may accommodate two additional metal atoms coordinated by the rest four triple bonds to form M₃/GDY (**Scheme 1c**). Thus, we investigate the stability of M₃/GDY by comparing the average adsorption energies (E_{ads}) of metal clusters (1 – 20 atoms) on GDY, with M covering groups VIII and IB TM elements, since they are usually considered as good catalyst candidates.



Scheme 1. Schematic Illustrations of (a) GDY, (b) M₁/GDY, and (c) M₃/GDY.

M_1/GDY is never the most stable case, but is surprisingly the most unstable for Fe, Co, Cu, Ru, Rh, Os, Ir, Pt, and Au on GDY, compared with their other-sized clusters. (**Figure 1**) This finding shakes the very foundation of all previous work on M_1/GDY . As expected, M_3/GDY is the most stable for all cases except Ag, Os, and Au. Taking Cu as an example, the E_{ads} ($E_{\text{ads}} = [E(M_x/\text{GDY}) - x \cdot E(\text{M, bulk}) - E(\text{GDY})]/x$, where x is the number of atoms composing the anchored cluster) of Cu_1 on GDY is 1.25 eV, but it decreases dramatically to the lowest value of 0.72 eV for Cu_3 . When adding one more Cu atom to Cu_3/GDY , E_{ads} increases to 0.95 eV. E_{ads} peaks at Cu_6 with a value of 1.22 eV, and starts to decrease to 0.91 eV at Cu_{20} , due to the formation of more metal-metal bonds. Thus, “three” is a magic number for the thermodynamic stability of these GDY-supported metal clusters. While in the Ag, Os, and Au cases, E_{ads} decreases from M_1 to M_{20} in general.

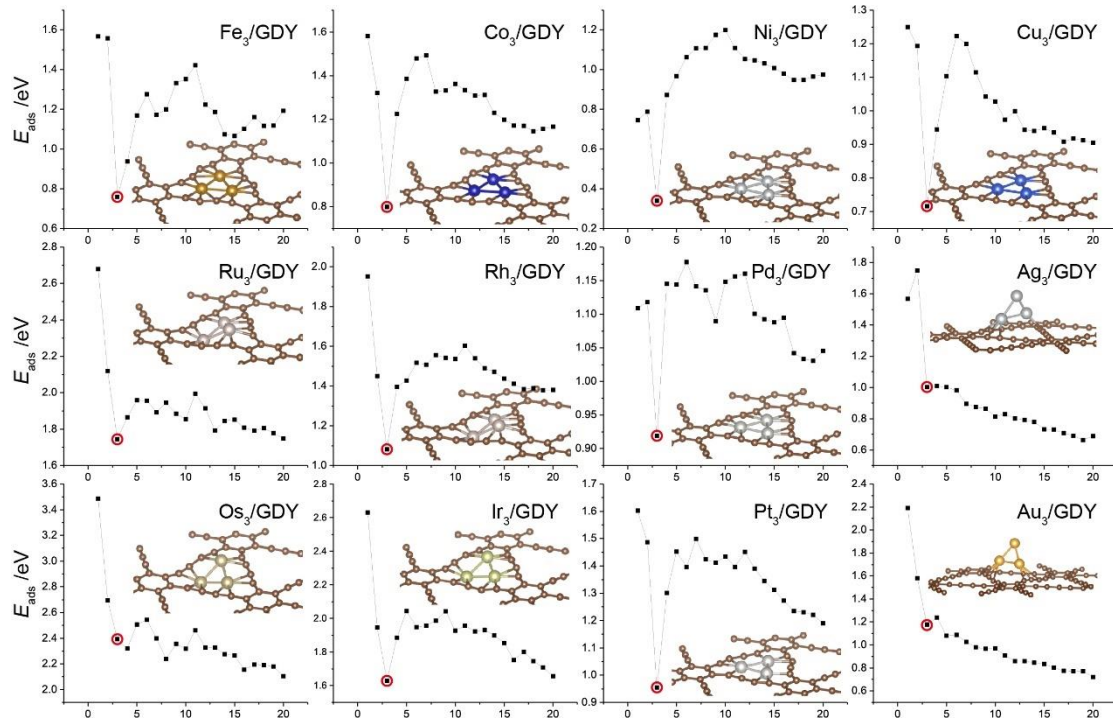


Figure 1. The average adsorption energies, $E_{\text{ads}} = [E(M_x/\text{GDY}) - x \cdot E(\text{M, bulk}) - E(\text{GDY})]/x$, of metal clusters with 1 – 20 atoms on GDY. The points for M_3/GDY are marked in red circles, and their structures are shown in the insets.

AIMD simulations and phonon dispersions of all M_3/GDY cases further characterize their kinetic stability (**Figures 2 and S1-5**). In the 15 ps AIMD trajectories, all M_3 clusters remain at the 18MR, except for Ag_3/GDY and Au_3/GDY . The root-mean-square deviations (RMSDs) of M_3 clusters are all at low levels with small fluctuations, indicating that no diffusion and decomposition occur within 15 ps. Taking Cu_3/GDY as an example, the coordination number (CN) of Cu to Cu (Cu-Cu) obtained from integrating the first peak of radial distribution function (RDF) is 2 with a bond length of 2.47 Å, which means that the triangular configuration is well kept in the AIMD trajectories. The CNs of Cu-C from integrating the first and second peaks of RDF are 2 and 4,

respectively, which are consistent with the statically optimized structures. Therefore, the M_3 /GDY is also stable from the dynamic aspect. The phonon spectrum, showing no imaginary frequency, further confirms the kinetic stability of Cu_3 /GDY. (**Figure 2d**)

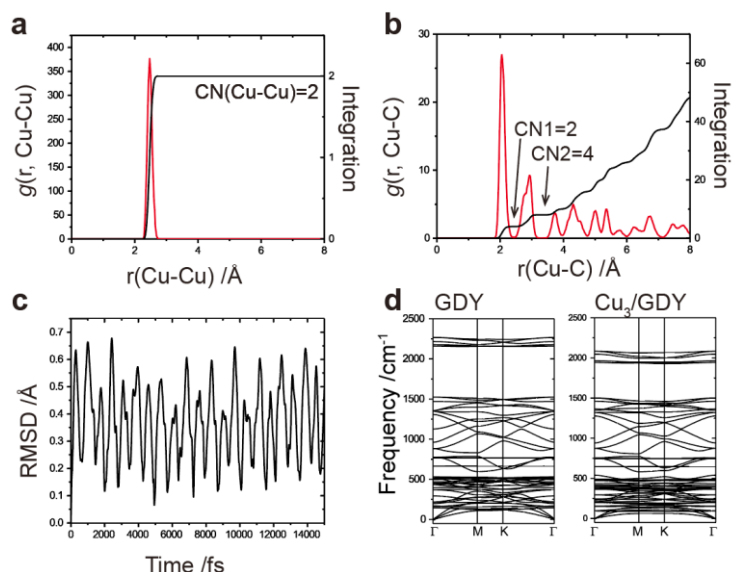


Figure 2. The AIMD simulation of Cu_3 /GDY: (a, b) The RDF and integrated RDF for Cu-Cu and Cu-C, and (c) the RMSD of M_3 cluster. (d) The predicted phonon spectra for GDY and Cu_3 /GDY.

The outstanding stability of M_3 /GDY enables the possibility of synthesizing them with our EcPW strategy, due to the presence of chemical potential windows that distinguish the trimer cluster form from the other-sized forms anchored on the GDY support. The stability of M_3 /GDY originates from the specific interactions between the metal trimer clusters and the GDY support, which can be analyzed and elucidated from geometries and electronic structures discussed in the following sections.

Geometries of M_3 /GDY.

Only with M_3 in the plane of GDY may M_3 /GDY retain the D_{3h} symmetry, but most of M_3 cannot fit into the 18MR-hole. The optimized M_3 /GDY structures show that only Cu_3 /GDY is of D_{3h} symmetry, and the rest M_3 /GDY structures are with distortions in both the GDY substrate and M_3 cluster. We summarize the three types of distortions as shown in **Figure 3a**. Type I distortion is with the rotation of both $C\equiv C$ bonds and M_3 within the GDY plane. Type II distortion is with the out-of-plane rotation of M_3 . Type III distortion is also with M_3 moving out of plane but with one metal atom detached from GDY.

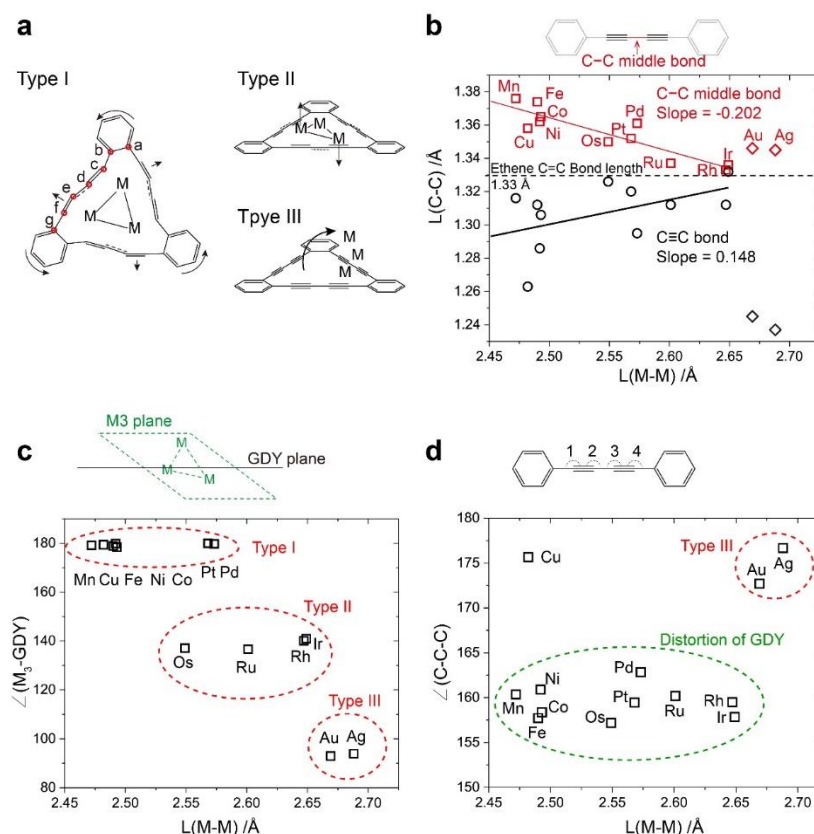


Figure 3. The distortions in structures of M₃/GDY. (a) Schematic illustrations of Type I, II, and III distortions. (b) Correlation of the C_d-C_e middle bond and C≡C triple bond lengths with metal-metal (M-M) bond length. (c) Correlation of the angle between M₃ plane and GDY plane with M-M bond length. (d) Correlation of the averaged angle of C-C-C on acetylenic linkages with M-M bond length.

The cases of Mn, Cu, Fe, Ni, Co, Pd, and Pt belong to Type I distortion, which is of C_{3h} symmetry. This distortion is due to either the mismatch between the 18MR-hole and M₃ or requirement by specific coordination. Take Pt as an example, $\angle(C_b-C_c-C_d)$ decreases from 180° to 143.7° with C_c approaching Pt₃ cluster. The electron localization function (ELF) shows a localized red region between Pt and C_c (**Figure 4g**), implying a typical d - σ covalent bond. Meanwhile, the hybridization of C_c changes from sp to sp² like. $\angle(C_d-C_e-C_f)$ also decreases from 180° to 145.7° with C_e going away from Pt₃ cluster. The ELF shows delocalized red regions between Pt and C_d, C_e, C_f, implying a d - π bond. The original two C≡C π bonds are weakened, and the average length of these bonds increases from 1.227 Å to 1.325 Å.

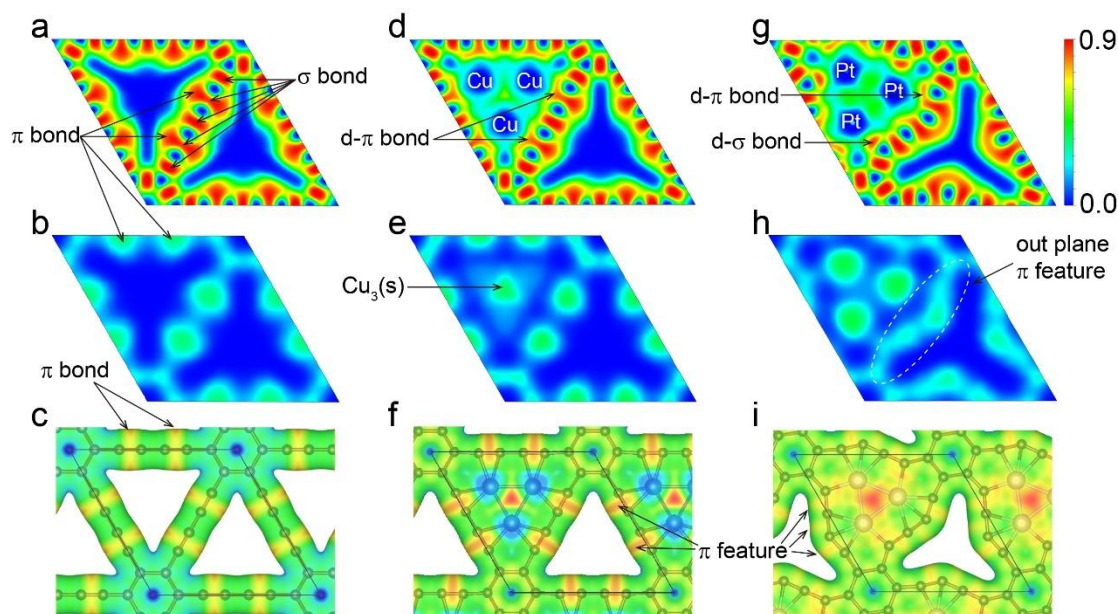


Figure 4. The 2D contour plots of electron localization function (ELF) for (a, b) GDY, (d, e) Cu₃/GDY, and (g, h) Pt₃/GDY at the GDY plane and 1.5 Å above it, respectively. The electrostatic-potential-colored charge density isosurfaces at 0.02 |e|/bohr³ for (c) GDY, (f) Cu₃/GDY, and (i) Pt₃/GDY, where the red region is dominated by electrons and the blue region is dominated by nuclei.

The cases of Ru, Rh, Os, and Ir belong to type II distortion, which has no symmetry. In this type, the size of M₃ cluster does not match well that of 18MR. The M-M bond lengths of these clusters (2.55 – 2.65 Å) are usually larger than those in type I (**Figure 3c**), and the angles between M₃ plane and GDY plane are around 140°. **Figure 3b** shows that the lengths of the original C≡C bonds increase to 1.31 – 1.33 Å, and the lengths of middle C-C bonds decrease to 1.33 – 1.35 Å, both converging to the C=C bond length of 1.33 Å in ethene. Thus, the π electrons of C≡C triple bonds in GDY are largely involved in the conjugated system in type II M₃/GDY. **Figure 3d** shows that both Type I and Type II distortions destroy the linear configuration of acetylenic linkages with an average bent angle of around 160°.

The cases of Ag and Au belong to type III distortion, in which M₃ is out of the GDY plane with only two of atoms coordinated to GDY and the rest one detached, and M₃ is almost vertical to the GDY plane. The M-M bond lengths of Au₃ and Ag₃ are 2.688 and 2.669 Å, respectively, which are too large to fit in the 18MR.

Electronic structures of M₃/GDY.

We further investigate the electronic structures of GDY, Cu₃/GDY, and Pt₃/GDY as representative cases. The ELF and electrostatic potential maps of GDY (**Figures 4a-c**) show that the six triple bonds of 18MR-hole provide localized π electrons (in the GDY plane) at the border, offering perfect anchor sites for TM atoms. In Cu₃/GDY (**Figures 4d, e**), each Cu atom indeed forms

two $d-\pi$ coordination bonds with the localized π systems of $C\equiv C$ bonds in the GDY plane, leaving the π systems perpendicular to the GDY plane intact. And the three 4s orbitals of Cu_3 form a three-center two-electron (3c-2e) bond with the bonding electrons localized above the center of Cu_3 (**Figure 4f**), which renders Cu_3 center as a potential nucleophilic SCC.

The band structures (**Figure 5**, **Figure S5**) show that the direct band gap of GDY is calculated to be 0.49 eV and 0.93 eV at PBE and HSE06 levels, respectively, in agreement with previous work.^{41, 53} The VBM of GDY is simply composed of the conjugated π system formed by the $C\equiv C$ bonds and benzene rings, with the corresponding π^* orbitals composing the CBM. In Cu_3 /GDY, two new bands appear between the original VBM and CBM, which are composed of the 3c-2e bond by Cu 4s orbitals and the $d-\pi$ anti-bonding orbitals. The rest 3d bands of Cu_3 are very narrow and localized between -2.0 to -3.2 eV below the Fermi level. The original CBM bands of GDY are partially occupied, due to the charge transfer from Cu_3 to GDY, indicating the metallic character of Cu_3 /GDY. The Bader charge of Cu_3 is $+1.21 |e|$, indicating that one 4s electron of Cu_3 is donated to GDY. Thus, the Cu_3 cluster is of +1 oxidation state, and the left two 4s bonding electrons forming the 3c-2e bond satisfy the Hückel $[4n + 2]$ rule, which is of typical aromatic feature. The analysis of molecular orbital interactions between GDY and Cu_3 is presented in **Figure S6**, which leads to similar conclusions.

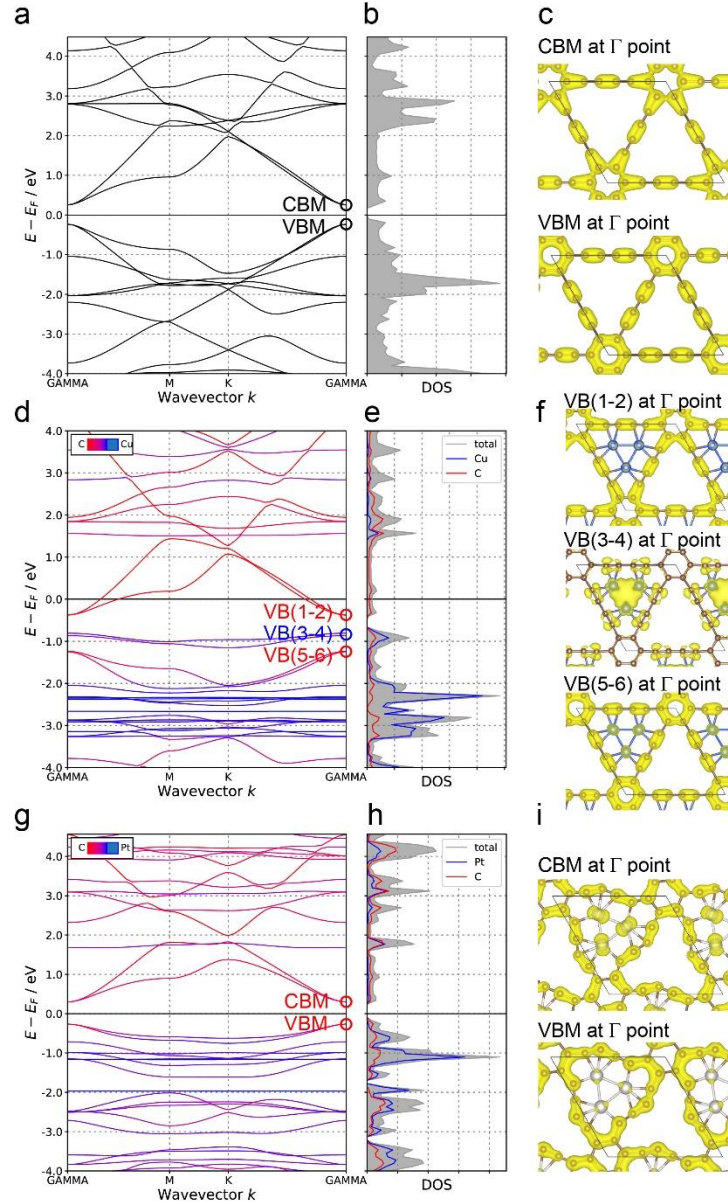


Figure 5. The band structures (Γ -M-K- Γ) and corresponding densities of states at PBE level for (a, b) GDY, (d, e) Cu_3/GDY , and (h, i) Pt_3/GDY . The partial charge density contours of (c) VBM and CBM of GDY, (f) VB (1-6) of Cu_3/GDY , and (i) VBM and CBM of Pt_3/GDY .

For Pt_3/GDY , the direct band gap is 0.56 eV and 0.63 eV at PBE and HSE06 levels, respectively. Different from Cu_3/GDY , there is no new band between the VBM and CBM of GDY. Instead, the 5d orbitals of Pt_3 are mixed into the GDY bands, as shown in the projected band structure and density of states. Such mixing leads to charge transfer from Pt_3 to GDY and strong bonding between Pt and C, reducing the $\text{C}\equiv\text{C}$ bonds of GDY into double bonds. The ICOHP of $\text{C}\equiv\text{C}$ bonds is reduced from -15.39 to -12.84 eV, and the ICOHP of $\text{C}_d\text{-C}_e$ single bonds increases from -11.70 to -12.72 eV (**Figure S7**). Thus, the bond strengths along the linkage become uniform, which is consistent with the bond length and angle analysis (**Figure 3**).

Catalytic performance.

Because of low oxidation states, the metal clusters of M_3 /GDY are electron-rich and thus are good candidate catalysts for reduction reactions. In addition, the GDY substrate can serve as an electron reservoir to buffer the oxidation state change of M_3 cluster during the catalytic reactions.⁵⁴ Here, we investigate the ORR, HER, and CO_2RR to demonstrate the catalytic capability of M_3 /GDY as a novel series of SCC.

It has been widely suggested that the adsorption energies of intermediates can characterize the whole catalytic performance. For example, the adsorption energies of key intermediates for HER and CO_2RR , $*H$ and $*COOH$, respectively, were normally employed to predict their overpotentials, and the adsorption energy of one of the intermediates for ORR, $*O$ or $*OH$, was commonly employed to predict the overpotential, because of the scaling relations among the adsorption energies of intermediates.⁵⁵⁻⁵⁶ Thus, we first investigate these intermediate adsorption energies, as well as the d -band center positions of metal clusters in M_3 /GDY. (**Figure 6**) Similar to their bulk counterparts, the late TM M_3 /GDY, such as Au, Ag, Cu, and Pt, have lower d -band center positions, and the adsorption energies of $*H$, $*O$, and $*COOH$ on them are weak. On the other hand, for Fe, Ru, Os, and Co, their d orbitals are partially occupied and thus their d -band center positions are higher in energy, leading to stronger adsorption for $*H$, $*O$, $*COOH$.

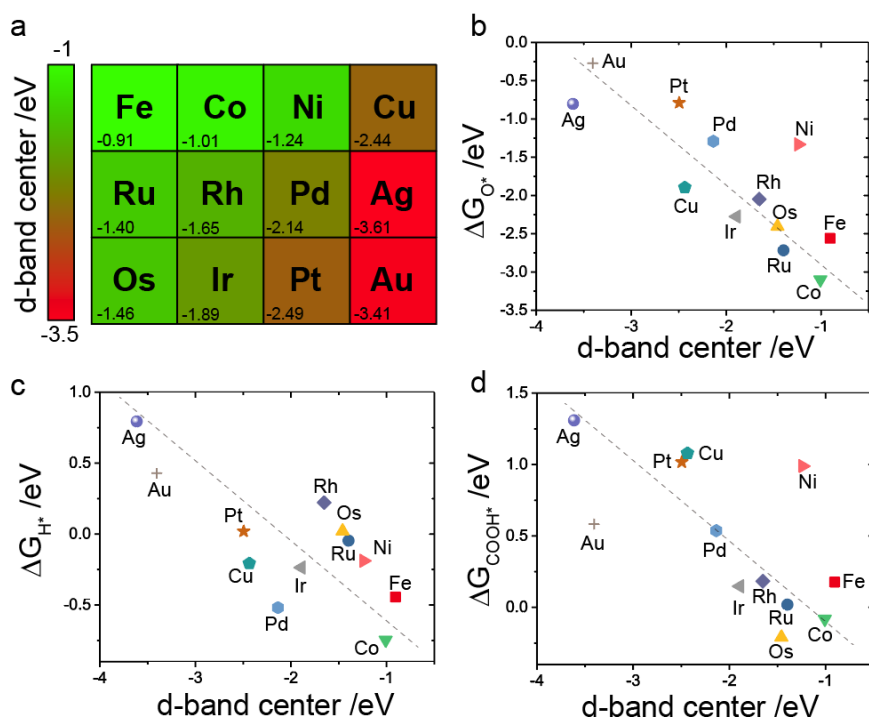


Figure 6. (a) The d -band center positions of metal clusters in M_3 /GDY. The correlation between the d -band center position and the adsorption energies for (b) O^* , (c) H^* , and (d) $COOH^*$.

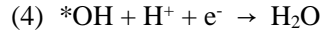
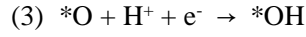
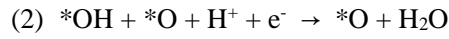
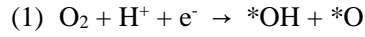
ORR. There are two distinct pathways for ORR.^{55, 57} One is the associative mechanism, where O_2

is first reduced to *OOH. The other is the dissociative mechanism, where O₂ dissociates first.

The associative mechanism: $O_2 + H^+ + e^- \rightarrow *OOH$;

The dissociative mechanism: $O_2 \rightarrow 2*O$, followed by $2*O + H^+ + e^- \rightarrow *OH + *O$.

We find that on all M₃/GDY, the dissociative adsorption of O₂ is thermodynamically favored over the molecular adsorption, and the *OOH species is thermodynamically unstable with respect to *O + *OH. Thus, the dissociated mechanism dominates on M₃/GDY, and the four electrochemical steps are:



Note that the dissociation of O₂, which is a chemical step, is integrated into the step (1), because we only consider the electrochemical steps here, based on the method by Nørskov et al.⁵⁵ **Figure 7b** summarizes the linear relationship between the reaction free energy ΔG for each electrochemical step and ΔG^*_{*O} . For the step (1), its ΔG increases as the ΔG^*_{*O} increases. But for the rest steps, their ΔG 's have negative slopes with respect to ΔG^*_{*O} .

The step (3) on all M₃/GDY has the highest ΔG as shown in **Figure 7b**, and thus it is always the potential limiting step (PLS) that determines the overpotential. This results in that the ORR on all M₃/GDY is on the same side of volcano plot. This is different from the corresponding series of metal surfaces, among which the Au and Ag surfaces are on the opposite side to the other metal surfaces, with Pt and Pd close to the top of volcano.⁵⁵ On Au and Ag surfaces, the step (1) is PLS, due to ΔG^*_{*O} higher than 2 eV. While the rest metal surfaces are similar to the M₃/GDY cases, with *O or *OH hydrogenation to be the PLS. This implies that the position of volcano top shifts to with higher ΔG^*_{*O} on M₃/GDY in comparison with metal surfaces. It is worth noting that the atomic utilization is 100% for M₃/GDY SCC, but is much lower for metal surface catalysts.

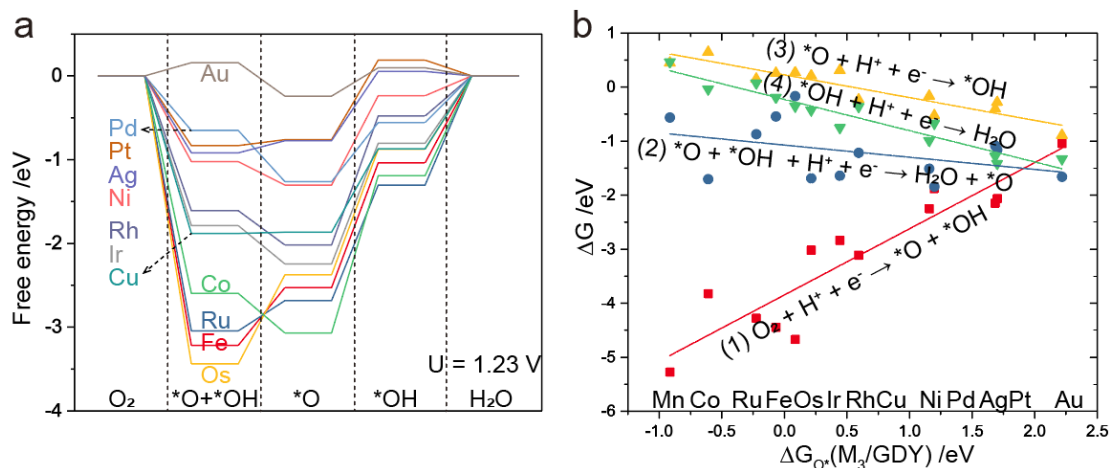
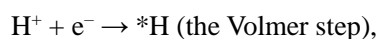
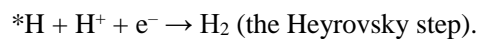
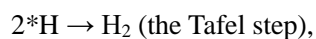


Figure 7. (a) The free energy diagrams for ORR at $U = 1.23$ V (vs SHE) on M_3/GDY . (b) The linear relationship between ΔG_{O^*} and ΔG for each electrochemical step on M_3/GDY .

HER. There are two distinct mechanisms for HER, the Volmer-Heyrovsky mechanism and the Volmer-Tafel mechanism. The first elementary reaction of both mechanisms provides the key intermediate $*H$ via the Volmer step,



in which the proton source H^+ can be either the solvated proton (e.g., the hydronium ion) or the water molecule. The second step can be either the combination of two $*H$ or the further hydrogenation of $*H$ by the proton source from the electrolyte,



On M_3/GDY , there is only one threefold hollow site to accommodate one $*H$. Thus, only the Volmer-Heyrovsky mechanism is viable, and the PLS is the step with larger ΔG . The predicted overpotentials for HER are lower than 0.05 V on Pt_3/GDY , Os_3/GDY , and Ru_3/GDY , which are potentially great catalyst candidates. **Figure 8b** compares the adsorption free energies of H atom (ΔG_{H^*}) on M_3/GDY and metal bulk surfaces, which show similar trends. ΔG_{H^*} on Au_3 and Ag_3 are too weak to drive the Volmer step, while ΔG_{H^*} on Co_3 , Pd_3 and Fe_3 are too strong to drive the Heyrovsky step.

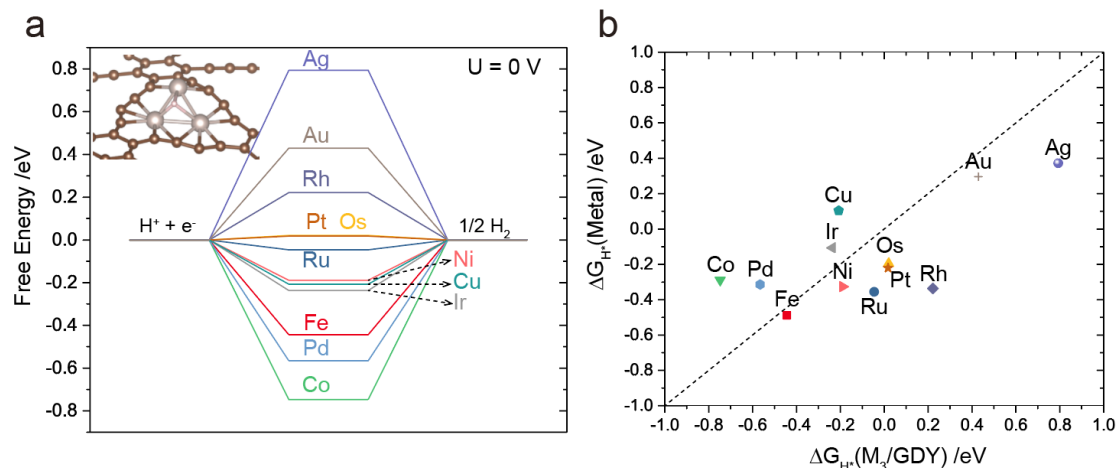
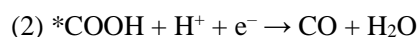
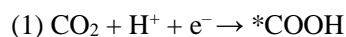


Figure 8. (a) The free energy diagrams for HER at U = 0 V (vs SHE) on M₃/GDY. (b) Comparison of ΔG_{H*} on metal bulk surfaces with those on M₃/GDY.

CO₂RR. Here, we also investigate the performance of M₃/GDY for CO₂RR with the mechanism as follows,⁵⁸



and the overall reaction free energy change is 0.21 eV. Similar to HER, the PLS is the step with larger ΔG. Different from on the metal surface, the *COOH adsorption on partially oxidized M₃ on GDY is not as stable. So, the first CO₂ hydrogenation step is the PLS for Ag₃/GDY, Cu₃/GDY, Pt₃/GDY, Ni₃/GDY, Au₃/GDY, Pd₃/GDY, Rh₃/GDY, Fe₃/GDY, Ir₃/GDY. But the *COOH hydrogenation step to produce the final product CO is the PLS for Ru₃/GDY, Co₃/GDY, and Os₃/GDY. **Figure 9** shows that the predicted overpotentials on Fe₃/GDY, Ir₃/GDY, Ru₃/GDY and Rh₃/GDY are lower than 0.1 V, implying high activity for CO₂RR. But Fe₃/GDY, Ir₃/GDY, Ru₃/GDY are not good candidates as CO₂RR catalysts, because they suffer from either the preferred adsorptions of *H over *COOH or the competing HER, and thus have selectivity problem. **Figure 9b** compares ΔG_{H*} with ΔG_{COOH*}, where the shadowed regions mark the HER and CO₂RR catalyst candidates with overpotentials lower than 0.1 V. In the left shadowed region (with Fe₃/GDY and Ir₃/GDY), the *H adsorption is more stable than *COOH, and it may proceed through the formic acid pathway (*H + CO₂ + e⁻ → HCOO⁻).⁵⁸ In the middle shadowed region (with Ru₃/GDY), the competing HER has comparable or higher activity with respect to CO₂RR, leading to poor selectivity. In the right shadowed region (with Rh₃/GDY), the high activity for CO₂RR dominates over that for HER, and thus Rh₃/GDY is an optimal candidate for highly efficient and selective CO₂RR.

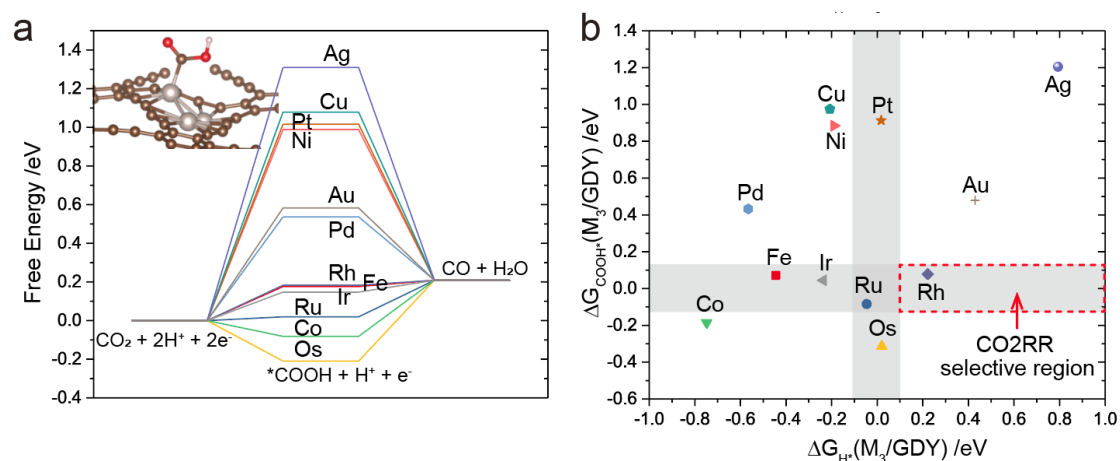


Figure 9. (a) Free energy diagrams for CO₂RR at U = 0 V (vs SHE) on M₃/GDY. (b) Comparison of ΔG_{H*} and ΔG_{COOH*} on M₃/GDY.

SUMMARY

By investigating both the thermodynamics and kinetics, we predict that the metal trimer cluster form anchored on GDY, i.e. M₃/GDY, is the most stable among all forms including the previously reported single-atom M₁/GDY for Fe, Co, Ni, Cu, Ru, Rh, Pd, Ir, and Pt. This lays the foundation for the synthesis of these M₃/GDY with our electrochemical potential window strategy. We further investigate the geometric and electronic structures to elucidate the specific interactions between the M₃ single-clusters and the GDY support that result in the extraordinary stability of M₃/GDY. More importantly, we propose this series of stable M₃/GDY as a novel and promising kind of SCCs with great potentials for efficient and precise heterogenous catalysis, and we demonstrate their catalytic performance for ORR, HER, and CO₂RR, which provide guidelines for practical applications.

ACKNOWLEDGMENTS

This work was financially supported by the National Natural Science Foundation of China (grant Nos. 91645203 and 21590792 to J.L. and grant No. 21903047 to H.X.). The support of Guangdong Provincial Key Laboratory of Catalysis (No. 2020B121201002) is also acknowledged. The calculations were performed using the supercomputers at Tsinghua National Laboratory for Information Science and Technology, the Computational Chemistry Laboratory of Department of Chemistry under Tsinghua Xuetang Talents Program, and the Supercomputer Center of Southern University of Science and Technology.

REFERENCES

1. Qiao, B.; Wang, A.; Yang, X.; Allard, L. F.; Jiang, Z.; Cui, Y.; Liu, J.; Li, J.; Zhang, T., Single-atom catalysis of CO oxidation using Pt₁/FeOx. *Nat. Chem.* **2011**, *3* (8), 634-641.
2. Yang, X.-F.; Wang, A.; Qiao, B.; Li, J.; Liu, J.; Zhang, T., Single-Atom Catalysts: A New Frontier in Heterogeneous Catalysis. *Acc. Chem. Res.* **2013**, *46*, 1740-1748.
3. Liu, J., Catalysis by Supported Single Metal Atoms. *ACS Catal.* **2017**, *7*, 34-59.
4. Wang, A.; Li, J.; Zhang, T., Heterogeneous single-atom catalysis. *Nat. Rev. Chem.* **2018**, *2*, 65-81.
5. Liu, J.-C.; Tang, Y.; Li, J.; Wang, Y.-G.; Zhang, T., Theoretical understanding of the stability of single-atom catalysts. *Natl. Sci. Rev.* **2018**, *5* (5), 638-641.
6. Liu, L.; Corma, A., Metal Catalysts for Heterogeneous Catalysis: From Single Atoms to Nanoclusters and Nanoparticles. *Chem. Rev.* **2018**, *118* (10), 4981-5079.
7. Zhang, S.; Nguyen, L.; Liang, J. X.; Shan, J.; Liu, J.; Frenkel, A. I.; Patlolla, A.; Huang, W.; Li, J.; Tao, F., Catalysis on singly dispersed bimetallic sites. *Nat. Commun.* **2015**, *6*, 7938.
8. Lei, Y.; Mehmood, F.; Lee, S.; Greeley, J.; Lee, B.; Seifert, S.; Winans, R. E.; Elam, J. W.; Meyer, R. J.; Redfern, P. C.; Teschner, D.; Schlogl, R.; Pellin, M. J.; Curtiss, L. A.; Vajda, S., Increased silver activity for direct propylene epoxidation via subnanometer size effects. *Science* **2010**, *328* (5975), 224-228.
9. Ji, S.; Chen, Y.; Fu, Q.; Chen, Y.; Dong, J.; Chen, W.; Li, Z.; Wang, Y.; Gu, L.; He, W.; Chen, C.; Peng, Q.; Huang, Y.; Duan, X.; Wang, D.; Draxl, C.; Li, Y., Confined Pyrolysis within Metal–Organic Frameworks To Form Uniform Ru₃ Clusters for Efficient Oxidation of Alcohols. *J. Am. Chem. Soc.* **2017**, *139* (29), 9795-9798.
10. Ma, X.-L.; Liu, J.-C.; Xiao, H.; Li, J., Surface Single-Cluster Catalyst for N₂-to-NH₃ Thermal

Conversion. *J. Am. Chem. Soc.* **2018**, *140* (1), 46-49.

11. Liu, J.-C.; Ma, X.-L.; Li, Y.; Wang, Y.-G.; Xiao, H.; Li, J., Heterogeneous Fe₃ single-cluster catalyst for ammonia synthesis via an associative mechanism. *Nat. Commun.* **2018**, *9* (1), 1610.

12. Wang, J.; Huang, Z.; Liu, W.; Chang, C.; Tang, H.; Li, Z.; Chen, W.; Jia, C.; Yao, T.; Wei, S.; Wu, Y.; Li, Y., Design of N-Coordinated Dual-Metal Sites: A Stable and Active Pt-Free Catalyst for Acidic Oxygen Reduction Reaction. *J. Am. Chem. Soc.* **2017**, *139* (48), 17281-17284.

13. Tjo, E. C.; Vajda, S., Catalysis by clusters with precise numbers of atoms. *Nat. Nanotech.* **2015**, *10*, 577-588.

14. Grundner, S.; Markovits, M. A. C.; Li, G.; Tromp, M.; Pidko, E. A.; Hensen, E. J. M.; Jentys, A.; Sanchez-Sanchez, M.; Lercher, J. A., Single-site trinuclear copper oxygen clusters in mordenite for selective conversion of methane to methanol. *Nat. Commun.* **2015**, *6*, 7546.

15. Li, Y.; Xu, L.; Liu, H.; Li, Y., Graphdiyne and graphyne: from theoretical predictions to practical construction. *Chem. Soc. Rev.* **2014**, *43* (8), 2572-2586.

16. Gao, X.; Liu, H.; Wang, D.; Zhang, J., Graphdiyne: synthesis, properties, and applications. *Chem. Soc. Rev.* **2019**, *48* (3), 908-936.

17. Huang, C.; Li, Y.; Wang, N.; Xue, Y.; Zuo, Z.; Liu, H.; Li, Y., Progress in Research into 2D Graphdiyne-Based Materials. *Chem. Rev.* **2018**, *118* (16), 7744-7803.

18. Haley, M. M.; Brand, S. C.; Pak, J. J., Carbon networks based on dehydrobenzoannulenes: synthesis of graphdiyne substructures. *Angewandte Chemie International Edition in English* **1997**, *36* (8), 836-838.

19. Zuo, Z.; Li, Y., Emerging Electrochemical Energy Applications of Graphdiyne. *Joule* **2019**,

3(4), 899-903.

20. Zhao, Y.; Tang, H.; Yang, N.; Wang, D., Graphdiyne: Recent Achievements in Photo- and Electrochemical Conversion. *Adv Sci (Weinh)* **2018**, *5* (12), 1800959.

21. Xue, Y.; Huang, B.; Yi, Y.; Guo, Y.; Zuo, Z.; Li, Y.; Jia, Z.; Liu, H.; Li, Y., Anchoring zero valence single atoms of nickel and iron on graphdiyne for hydrogen evolution. *Nat. Commun.* **2018**, *9* (1), 1460.

22. Li, X.; Xing, D., Systematic Theoretical Study of Electronic Structures and Stability of Transition-Metal-Adsorbed Graphdiyne Clusters. *Journal of Materials Chemistry C* **2019**, *123* (14), 8843–8850.

23. Hui, L.; Xue, Y.; Yu, H.; Liu, Y.; Fang, Y.; Xing, C.; Huang, B.; Li, Y., Highly Efficient and Selective Generation of Ammonia and Hydrogen on a Graphdiyne-Based Catalyst. *J. Am. Chem. Soc.* **2019**, *141* (27), 10677-10683.

24. Xu, G.; Wang, R.; Ding, Y.; Lu, Z.; Ma, D.; Yang, Z., First-Principles Study on the Single Ir Atom Embedded Graphdiyne: An Efficient Catalyst for CO Oxidation. *J. Phys. Chem. C* **2018**, *122* (41), 23481-23492.

25. He, T.; Matta, S. K.; Du, A., Single tungsten atom supported on N-doped graphyne as a high-performance electrocatalyst for nitrogen fixation under ambient conditions. *Phys. Chem. Chem. Phys.* **2019**, *21* (3), 1546-1551.

26. Yin, X. P.; Wang, H. J.; Tang, S. F.; Lu, X. L.; Shu, M.; Si, R.; Lu, T. B., Engineering the Coordination Environment of Single-Atom Platinum Anchored on Graphdiyne for Optimizing Electrocatalytic Hydrogen Evolution. *Angew. Chem. Int. Ed. Engl.* **2018**, *57* (30), 9382-9386.

27. Gao, Y.; Cai, Z.; Wu, X.; Lv, Z.; Wu, P.; Cai, C., Graphdiyne-Supported Single-Atom-Sized

Fe Catalysts for the Oxygen Reduction Reaction: DFT Predictions and Experimental Validations. *ACS Catal.* **2018**, *8* (11), 10364-10374.

28. Li, X.; Li, S., Investigations of electronic and nonlinear optical properties of single alkali metal adsorbed graphene, graphyne and graphdiyne systems by first-principles calculations. *Journal of Materials Chemistry C* **2019**, *7* (6), 1630-1640.

29. He, T.; Matta, S. K.; Will, G.; Du, A., Transition-Metal Single Atoms Anchored on Graphdiyne as High-Efficiency Electrocatalysts for Water Splitting and Oxygen Reduction. *Small Methods* **2019**, 1800419.

30. Seif, A.; López, M. J.; Granja-DelRío, A.; Azizi, K.; Alonso, J. A., Adsorption and growth of palladium clusters on graphdiyne. *Phys. Chem. Chem. Phys.* **2017**, *19* (29), 19094-19102.

31. Liu, J.-C.; Xiao, H.; Li, J., Constructing High-Loading Single-Atom/Cluster Catalysts via an Electrochemical Potential Window Strategy. *J. Am. Chem. Soc.* **2020**, *142* (7), 3375-3383.

32. Ma, D.; Zeng, Z.; Liu, L.; Huang, X.; Jia, Y., Computational Evaluation of Electrocatalytic Nitrogen Reduction on TM Single-, Double-, and Triple-Atom Catalysts (TM = Mn, Fe, Co, Ni) Based on Graphdiyne Monolayers. *J. Phys. Chem. C* **2019**, *123* (31), 19066-19076.

33. Zhang, H.; Xia, Y.; Bu, H.; Wang, X.; Zhang, M.; Luo, Y.; Zhao, M., Graphdiyne: A promising anode material for lithium ion batteries with high capacity and rate capability. *J. Appl. Phys.* **2013**, *113* (4), 044309.

34. Qi, H.; Yu, P.; Wang, Y.; Han, G.; Liu, H.; Yi, Y.; Li, Y.; Mao, L., Graphdiyne oxides as excellent substrate for electroless deposition of Pd clusters with high catalytic activity. *J. Am. Chem. Soc.* **2015**, *137* (16), 5260-5263.

35. Xing, D.-H.; Xu, C.-Q.; Wang, Y.-G.; Li, J., Heterogeneous Single Cluster Catalysts for

Selective Semi-Hydrogenation of Acetylene with Graphdiyne-Supported Triatomic Clusters. *J. Phys. Chem. C* **2019**, *123* (16), 10494-10500.

36. Ikuno, T.; Grundner, S.; Jentys, A.; Li, G.; Pidko, E.; Fulton, J.; Sanchez-Sanchez, M.; Lercher, J. A., Formation of Active Cu-oxo Clusters for Methane Oxidation in Cu-Exchanged Mordenite. *J. Phys. Chem. C* **2019**, *123* (14), 8759-8769.

37. Kresse, G.; Joubert, D., From ultrasoft pseudopotentials to the projector augmented-wave method. *Phys. Rev. B: Condens. Matter Mater. Phys.* **1999**, *59* (3), 1758.

38. Kresse, G.; Furthmüller, J., Efficient iterative schemes for ab initio total-energy calculations using a plane-wave basis set. *Phys. Rev. B: Condens. Matter Mater. Phys.* **1996**, *54* (16), 11169.

39. Kresse, G.; Furthmüller, J., Efficiency of ab-initio total energy calculations for metals and semiconductors using a plane-wave basis set. *Comput. Mater. Sci.* **1996**, *6* (1), 15-50.

40. Perdew, J. P.; Burke, K.; Ernzerhof, M., Generalized gradient approximation made simple. *Phys. Rev. Lett.* **1996**, *77* (18), 3865.

41. Long, M.; Tang, L.; Wang, D.; Li, Y.; Shuai, Z., Electronic structure and carrier mobility in graphdiyne sheet and nanoribbons: theoretical predictions. *ACS nano* **2011**, *5* (4), 2593-2600.

42. Wang, V.; Xu, N.; Liu, J.-C., VASPKIT: A Pre- and Post-Processing Program for the VASP Code., VASPKIT: A Pre- and Post-Processing Program for the VASP Code.
<http://vaspkit.sourceforge.net>.

43. Liu, H.; Wang, Y.; Bowman, J. M., Vibrational Analysis of an Ice Ih Model from 0 to 4000 cm⁻¹ Using the Ab Initio WHBB Potential Energy Surface. *J. Phys. Chem. B* **2013**, *117* (34), 10046-10052.

44. Bertie, J. E.; Whalley, E., Optical Spectra of Orientationally Disordered Crystals. II. Infrared Spectrum of Ice Ih and Ice Ic from 360 to 50 cm⁻¹. *J. Chem. Phys.* **1967**, *46* (4), 1271-1284.
45. Nosé, S., A unified formulation of the constant temperature molecular dynamics methods. *J. Chem. Phys.* **1984**, *81* (1), 511.
46. Hoover, W. G., Canonical dynamics: Equilibrium phase-space distributions. *Phys. Rev. A* **1985**, *31* (3), 1695-1697.
47. Baroni, S.; de Gironcoli, S.; Dal Corso, A.; Giannozzi, P., Phonons and related crystal properties from density-functional perturbation theory. *Reviews of Modern Physics* **2001**, *73* (2), 515-562.
48. Togo, A.; Tanaka, I., First principles phonon calculations in materials science. *Scripta Mater.* **2015**, *108*, 1-5.
49. Heyd, J.; Scuseria, G. E.; Ernzerhof, M., Erratum: "Hybrid functionals based on a screened Coulomb potential" [J. Chem. Phys. 118, 8207 (2003)]. *J. Chem. Phys.* **2006**, *124* (21), 219906.
50. Maintz, S.; Deringer, V. L.; Tchougréeff, A. L.; Dronskowski, R., LOBSTER: A tool to extract chemical bonding from plane-wave based DFT. *J. Comput. Chem.* **2016**, *37* (11), 1030-1035.
51. Deringer, V. L.; Tchougréeff, A. L.; Dronskowski, R., Crystal orbital Hamilton population (COHP) analysis as projected from plane-wave basis sets. *J. Phys. Chem. A* **2011**, *115* (21), 5461-5466.
52. ADF2019, S., Theoretical Chemistry, Vrije Universiteit, Amsterdam, The Netherlands, <http://www.scm.com>.
53. Tan, X.; Shao, H.; Hu, T.; Liu, G.; Jiang, J.; Jiang, H., High thermoelectric performance in

two-dimensional graphyne sheets predicted by first-principles calculations. *Phys. Chem. Chem.*

Phys. **2015**, *17* (35), 22872-81.

54. Li, X. F.; Li, Q. K.; Cheng, J.; Liu, L.; Yan, Q.; Wu, Y.; Zhang, X. H.; Wang, Z. Y.; Qiu, Q.;

Luo, Y., Conversion of Dinitrogen to Ammonia by FeN₃-Embedded Graphene. *J. Am. Chem.*

Soc. **2016**, *138* (28), 8706-9.

55. Nørskov, J. K.; Rossmeisl, J.; Logadottir, A.; Lindqvist, L.; Kitchin, J. R.; Bligaard, T.;

Jónsson, H., Origin of the Overpotential for Oxygen Reduction at a Fuel-Cell Cathode. *J. Phys.*

Chem. B **2004**, *108* (46), 17886-17892.

56. Nørskov, J. K.; Bligaard, T.; Logadottir, A.; Kitchin, J.; Chen, J. G.; Pandelov, S.; Stimming,

U., Trends in the exchange current for hydrogen evolution. *J. Electrochem. Soc.* **2005**, *152* (3),

J23-J26.

57. Seh, Z. W.; Kibsgaard, J.; Dickens, C. F.; Chorkendorff, I.; Nørskov, J. K.; Jaramillo, T. F.,

Combining theory and experiment in electrocatalysis: Insights into materials design. *Science*

2017, *355* (6321).

58. Cheng, T.; Xiao, H.; Goddard, W. A., Reaction Mechanisms for the Electrochemical

Reduction of CO₂ to CO and Formate on the Cu(100) Surface at 298K from Quantum

Mechanics Free Energy Calculations with Explicit Water. *J. Am. Chem. Soc.* **2016**, *138* (42),

13802-13805.